

Surface Modification of 304L Stainless Steel and Interface Engineering by HiPIMS Pre-Treatment

Angélique Chabanon, Alexandre Michau, Michel Schlegel, Deniz Gündüz, Beatriz Puga, Frédéric Miserque, Frédéric Schuster, Hicham Maskrot, Cristelle Pareige, Emmanuel Cadel, et al.

▶ **To cite this version:**

Angélique Chabanon, Alexandre Michau, Michel Schlegel, Deniz Gündüz, Beatriz Puga, et al.. Surface Modification of 304L Stainless Steel and Interface Engineering by HiPIMS Pre-Treatment. Coatings, 2022, 12 (6), 10.3390/coatings12060727 . hal-03682342

HAL Id: hal-03682342

https://normandie-univ.hal.science/hal-03682342

Submitted on 31 May 2022

HAL is a multi-disciplinary open access archive for the deposit and dissemination of scientific research documents, whether they are published or not. The documents may come from teaching and research institutions in France or abroad, or from public or private research centers.

L'archive ouverte pluridisciplinaire **HAL**, est destinée au dépôt et à la diffusion de documents scientifiques de niveau recherche, publiés ou non, émanant des établissements d'enseignement et de recherche français ou étrangers, des laboratoires publics ou privés.

coatings

MDPI

Article

Surface Modification of 304L Stainless Steel and Interface Engineering by HiPIMS Pre-Treatment

Angélique Chabanon [1,2], Alexandre Michau [1], Michel Léon Schlegel [1,*], Deniz C. Gündüz [1], Beatriz Puga [3], Frédéric Miserque [3], Frédéric Schuster [4], Hicham Maskrot [1], Cristelle Pareige [5], Emmanuel Cadel [5], Georges Beainy [6], Véronique Cloute-Cazalaa [6], Srikanth Narasimalu [7], Bingqing Yao [8], Zhili Dong [8] and Fanny Balbaud-Célérier [3]

1 Service d'Études Analytiques et de Réactivité des Surfaces, Université Paris-Saclay, CEA, 91191 Gif-sur-Yvette, France; ang.chabanon@gmail.com (A.C.); alexandre.michau@gmail.com (A.M.); deniz.gunduz@ensicaen.fr (D.C.G.); hicham.maskrot@cea.fr (H.M.)
2 Interdisciplinary Graduate School, Nanyang Technological University, Singapore 637371, Singapore
3 Service de la Corrosion et du Comportement des Matériaux dans leur Environnement, Université Paris-Saclay, CEA, 91191 Gif-sur-Yvette, France; beatriz.puga@cea.fr (B.P.); frederic.miserque@cea.fr (F.M.); fanny.balbaud@cea.fr (F.B.-C.)
4 Cross-Cutting Program on Materials and Processes Skills, Université Paris-Saclay, CEA, 91191 Gif-sur-Yvette, France; frederic.schuster@cea.fr
5 Groupe de Physique des Matériaux, UMR 6634 CNRS, Université de Rouen Normandie et INSA de Rouen Normandie, Avenue de l'Université, 76801 Saint-Etienne-du-Rouvray, France; cristelle.pareige@univ-rouen.fr (C.P.); emmanuel.cadel@univ-rouen.fr (E.C.)
6 Service d'Etudes des Matériaux Irradiés, Université Paris-Saclay, CEA, 91191 Gif-sur-Yvette, France; georges.beainy@cea.fr (G.B.); veronique.cloute-cazalaa@cea.fr (V.C.-C.)
7 Energy Research Institute@NTU, Nanyang Technological University, Singapore 639798, Singapore; nsrikanth@ntu.edu.sg
8 School of Materials Science and Engineering, Nanyang Technological University, Singapore 639798, Singapore; yaob0004@e.ntu.edu.sg (B.Y.); zldong@ntu.edu.sg (Z.D.)
* Correspondence: michel.schlegel@cea.fr; Tel.: +33-169-084-836

Abstract: A clean and defect-free substrate/coating interface is required to guarantee good adhesion of coatings under service conditions. For this purpose, an etching pre-treatment using High-Power Impulse Magnetron Sputtering (HiPIMS) was performed to modify the surface of 304L stainless steel. The effect of three etching procedures on the substrate properties, such as corrosion resistance and adhesion, was investigated with unprecedented spatial resolution and spectroscopic details. Glancing angle X-ray diffraction showed modification in phase content but no neoformation after steel etching. X-ray photoelectron spectroscopy confirmed the presence of etchant species (6–7 at.%) on the extreme surface of the substrate. Transmission Electron Microscopy and Atomic Probe Tomography showed that the interface was less than a few nanometers wide. Polarization curves in a nitric acid solution at boiling temperature showed, for the first time, that the Ti^+ and Zr^+ etchings decreased the corrosion current density compared to the untreated original surface. Scratch-test measurements indicated better substrate/coating adhesion using HiPIMS metal ion etching. Electrochemical characterization revealed that Zr etching and thin coating improve the anti-corrosion properties of stainless steel in strong nitric acid conditions.

Keywords: 304L stainless steel; HiPIMS; GA-XRD; TEM; APT; etching; corrosion resistance; adhesion

check for updates

Citation: Chabanon, A.; Michau, A.; Schlegel, M.L.; Gündüz, D.C.; Puga, B.; Miserque, F.; Schuster, F.; Maskrot, H.; Pareige, C.; Cadel, E.; et al. Surface Modification of 304L Stainless Steel and Interface Engineering by HiPIMS Pre-Treatment. *Coatings* **2022**, *12*, 727. https://doi.org/10.3390/coatings12060727

Academic Editor: Emanuele Galvanetto

Received: 26 April 2022
Accepted: 20 May 2022
Published: 25 May 2022

Publisher's Note: MDPI stays neutral with regard to jurisdictional claims in published maps and institutional affiliations.

Copyright: © 2022 by the authors. Licensee MDPI, Basel, Switzerland. This article is an open access article distributed under the terms and conditions of the Creative Commons Attribution (CC BY) license (https://creativecommons.org/licenses/by/4.0/).

1. Introduction

Nowadays, improving the durability, performance and lifetime of industrial equipment is essential for carbon-free energy infrastructures. This is the case for nuclear fuel reprocessing plants using concentrated nitric acid [1,2]. For many components exposed to corrosive environments, austenitic stainless steels (304L) are used, whereas specific

alloys such as zirconium 702 alloy can be considered for the most critical parts. In this environment, a stable Cr-based passive layer protects the 304L stainless steel. However, deterioration of this protective layer may lead to significant corrosion [3]. Consequently, improvement in corrosion resistance properties, *e.g.*, by protective coatings, is necessary to extend the lifespan of 304L steel in nitric acid.

The development of environmentally friendly, industrially and economically viable surface treatments for improving sustainability is a challenging task. For this purpose, architectural coating systems (substrate/metallic bond coat/ceramic coating) are proposed to increase the lifespan of austenitic stainless steel. Various types of coatings, including ceramic ones, have been investigated [4–18]. In the past few years, these thin coatings have been elaborated by various physical vapor deposition (PVD) techniques, most notably by reactive magnetron sputtering [6,7,19]. The deposition of protective coatings may be further optimized using High Power impulse Magnetron Sputtering (HiPIMS) [20]. This PVD technique is based on the sputtering of a target by a plasma created by high power pulses in a plasmagenic atmosphere, *e.g.*, Ar. Ionized Ar sputters and ejects target atoms, which are then partially ionized in the plasma. A high-density plasma with a high ionization fraction of the sputtered species is then obtained in the cathode vicinity [21–25]. The composition of the ionized vapor can be optimized by tuning sputtering parameters, for example, with the help of *in situ* monitoring tools such as optical spectroscopy. Next, the plasma properties can be used for tweaking interesting properties of the coatings [26,27]. Improved control of coating composition, microstructure and mechanical properties is achieved through high ion-to-neutral ratios and intense ionic bombardment [22,26]. However, the overall performance of the coating system not only depends on the coating itself but also on the substrate surface pre-treatment as well as the coating architecture (*i.e.*, bond coat/interlayer and/or multilayer).

To overcome this issue, the coating system has to be optimized step-by-step: etching pre-treatment, deposition of the interlayer/bond coat and then coating deposition. It has been recognized that corrosion is mainly initiated by coating defects (pores, pinholes or scratches) and species trapped at the substrate/coating system interfaces [4,27,28]. Thus, defect-free interfaces should improve adhesion and anticorrosive properties [26,27]. In HiPIMS, these defect-free interfaces can be obtained by etching the surface with ions both from the plasmogenic gas Ar and from the target [23,29]. These ions are accelerated toward the surface by an important substrate bias (voltage greater than 800 V) [30,31]. They remove contaminants and impurities from the surface and may also be implanted in the substrate. This implantation is enhanced at a very important voltage and substantially modifies the surface composition, microstructure and corrosion properties [32,33]. In addition, in some cases, such as possible lack of adhesion due to different thermal expansion coefficients and mismatched crystal lattices, a bond coat is often required to allow coating adhesion, especially for ceramic coatings [30,34]. Hence, optimization of the substrate/coating interface is a processing route to improve the performance of the coated component under service conditions.

This work scrutinizes the preparation of stainless steel surfaces prior to HiPIMS coating. The strategy followed in this work starts with investigating the effect of an ion etching pre-treatment (argon and metal ions) on 304L stainless steel by HiPIMS from titanium or zirconium targets in order to assess the gain obtained with this process compared to Ar etching. The main objective is to form a clean, defect-free and as dense as possible interface, leading to the highest adhesion strength. Focus is placed on the influence of the etchant ions type on the substrate surface. First, the composition and structure of the modified substrate surfaces were analyzed by implementing a combination of spectroscopic, structural and microscopic techniques down to the atomic-scale resolution. Then, measurements of the substrate/metallic bond coat adhesion were performed to correlate structural and mechanical properties. The corrosion behavior of the etched samples and etched and metallic bond coat-deposited samples was evaluated in a nitric acid solution at boiling temperature using potentiodynamic polarization. Finally, the electrochemically investigated surface was

characterized to unravel the crystallochemical foundations of the observed phenomena. The results provide an original and extensive insight into the effect of the etching step on the surface modification of the 304L stainless steel substrate as well as the properties of the substrate/metallic bond coat system.

2. Materials and Methods

2.1. Materials and Surface Treatment

Commercial 304L austenitic stainless steel (Icaunaise des métaux, Véron, France) with an hyperquenching heat treatment at 1050 °C was received as stripes. The nominal composition of the 304L stainless steel in this work was obtained by Glow Discharge Mass Spectrometry (GDMS) using an Element GD Plus spectrometer (Thermo Scientific, Waltham, MA, USA) and is given in Table 1. The 304L austenitic stainless steel studied in this project displays an austenitic matrix of face-centered cubic (fcc) type (≈98%) and small amounts of body-centered cubic (bcc) ferrite (≈2%) as well as grain size of 22 ± 9 µm.

Table 1. Chemical composition of 304L stainless steel measured by GDMS.

Elements	C	Mn	P	Si	S	Cr	Ni	Cu	Co	N	Fe
wt.%	0.014	1.33	0.03	0.42	0.001	17.73	9.82	0.32	0.125	0.001	balance

Coupons (30 × 20 × 1.5 mm) with a suspension hole (1.5 mm Ø) were polished using SiC abrasive discs up to 4000 grit and then ultrasonically cleaned in acetone and ethanol prior to ion etching. Plasma etching by Ar^+, Ti^+ or Zr^+ was performed in a HiPIMS chamber developed by DEPHIS (Etupes, France). The chamber is equipped with Ti or Zr rectangular targets (636 × 127 mm, 99.9% purity) manufactured by Nano & Micro PVD (Etupes, France). During the first etching experiment, namely Ar^+, negative direct current (DC) bias was applied to the substrate holder (−900 V and 2500 W) for 20 min with an Ar partial pressure (p(Ar)) of 1.0 Pa. For the second (Ti^+) and third (Zr^+) etching experiments, unipolar pulses were sent onto the Ti or Zr target for 20 min with a p(Ar) of 0.6 Pa and a comparable DC bias (−900 V and 2500 W) was applied to the substrate holder. For Ti^+ and Zr^+ etchants, the targets were powered using a GX100/1000 DC power supply (ADL Analoge & Digitale Leistungselektronik GmbH, Darmstadt, Germany) combined with a SPIK3000A pulsing unit (MELEC GmbH, Baden-Baden, Germany). The average power, frequency, pulse duration and duty cycle for each cathode were set at 2500 W, 250 Hz, 20 µs and 1%, respectively. A metallic bond coat (Ti or Zr) was deposited by HIPIMS after the etching step to allow finer characterizations of the substrate/coating interface and the study of the corrosion resistance of a substrate/metallic bond coat system. During the metallic bond coat deposition, unipolar pulses were sent onto the Ti or Zr target for 100 min with a p(Ar) of 0.6 Pa, and a comparable DC bias (−100 V and 2000 W) was applied to the substrate holder. The average power, frequency, pulse duration and duty cycle for each cathode were set at 2000 W, 500 Hz, 50 µs and 5%, respectively. Samples were suspended at a distance of about 9 cm from the Ti or Zr target. The etching and deposition steps were performed in a static configuration in order to limit contamination of the sample surfaces observed during the previous etchings in a triple rotation configuration. This contamination was due to the resputtering of residues on the substrate holder and the walls of the deposition chamber. Note that in the final architectural coating system, the metallic bond coat acts as an interlayer between the 304L substrate and the coating.

The implanted depth and the distribution profiles of Ar, Ti and Zr in the 304L stainless steel substrate were modeled using the SRIM-2013 software [35,36]. SRIM calculations were performed by approximating the ion bombarding energy [36] to 900 eV, corresponding to the negative DC bias value applied to the substrate holder [37]. In addition, the ion incidence was fixed to the direction normal to the substrate. Note that the software cannot model the simultaneous bombardment of several ions at variance with experimental

conditions. The total number of incident ions was set to 10^4 in order to obtain a better statistical accuracy on the penetration depth.

2.2. Materials Characterization Techniques

The crystalline structure was investigated by Glancing Angle X-ray Diffraction (GAXRD) on a limited sample depth (a few micrometers to a few nanometers) using a D8 Advance diffractometer (Bruker, Karlsruhe, Germany) with Cu-Kα radiation ($\lambda_{K\alpha}$ = 1.540 Å, 40 kV, 40 mA), an incident angle of 0.5° and a Lynxeye® linear detector (Bruker). At this incident angle, the penetration depth of X-rays, as estimated with the AbsorbDX software (Bruker, Karlsruhe, Germany, version 3), amounts to about 95 nm for 304L ASS, 220 nm for Ti and 227 nm for Zr. Data acquisition and processing were performed using the DIFFRAC.SUITE software (Bruker) and the Joint Committee on Powder Diffraction Standards (JCPDS) database.

The chemical composition and chemical environment of each element on the extreme surface (1 to 10 nm depth) were studied by X-ray Photoelectron Spectroscopy (XPS) using an Escalab 250 XI spectrometer (Thermo Fisher Scientific, Waltham, MA, USA) equipped with a monochromatic X-ray Al-Kα source (hν = 1486.6 eV). The diameter of the analytical spot size is 900 µm. The energy was calibrated using the Fermi level (0 eV) and the Ag 3d5/2 level (368.3 eV) of silver. The high-resolution spectra were recorded using a constant pass energy of 20 eV. In addition, XPS depth profiles were recorded using Ar^+ ions at 1 keV for surface erosion. Data processing was performed with the commercial software Avantage (Thermo Fisher Scientific) by applying a Shirley-type background to all spectra.

The nanometer-scale microstructure and composition of the substrate/coating interface were investigated by Transmission Electron Microscopy (TEM) using a JEM 2100F (JEOL, Tokyo, Japan) operated at 200 kV and equipped with an Energy Dispersive X-ray (EDX) analyzer (EDAX Mahwah, NJ, USA). The $\leq$100 nm-thick samples were previously prepared using the Focus Ion Beam (FIB) technique in a Crossbeam 540 microscope (ZEISS, Oberkochen, Germany).

Two atomic-scale composition analyses of the etched samples were performed by Atom Probe Tomography (APT). The first analyses were carried out at CEA/DMN using a LEAP 4000X HR (CAMECA, Genevilliers, France) instrument in laser mode with an energy of 50 pJ and a room temperature of 60 K. Data processing was performed with the IVAS 3.6.12 (CAMECA) software. The APT tips were prepared with a Helios 650 NanoLab (FEI, Hillsboro, OR, USA) microscope equipped with a Ga ion source operating in the accelerating voltage range from 0.5 to 30 kV. The second APT measurement was conducted in electrical mode with a pulse fraction of 15% at 60 K. Volume reconstruction was performed using IVAS 3.8.0. Data processing was carried out with the 3D APT data software developed by the GPM research group in Rouen, France. The APT tips were prepared with a Helios (Thermo Fisher Scientific, Waltham, MA, USA) plasma FIB dual beam microscope.

2.3. Electrochemical Techniques

Electrochemical measurements were performed using a classical three-electrode configuration in a 250 mL FlatCell® (BioLogic, Seyssinet-Pariset, France). The electrolyte was a nitric acid solution (2.50 mol/L HNO_3, 2.50 mol/L $NaNO_3$ and 4.95×10^{-3} mol/L $Fe(NO_3)_3$) at boiling temperature (110 °C). A platinum wire was used as a counter electrode, and a saturated Hg/Hg_2SO_4 (E = 0.658 V/standard hydrogen electrode (SHE) at 25 °C) as a reference electrode, shielded from the acid solution by a triple salt bridge because of the harsh environment and high temperature. Using a polymer sample holder and a conductive screw, the reacting surface of the modified substrate was pressed against a rubber joint on one side of the cell so that 1 cm^2 of the surface was exposed to the solution and acted as a working electrode. For the easiest comparison with literature data, all potentials in this work are quoted versus the SHE.

First, open circuit potential (E_{OCP}) was monitored for 6 h to evaluate the stability of the working electrode potential. Then, an anodic polarization was performed at a rate of

0.2 mV/s from −0.03 to +0.5 V/E_{OCP}. This E_{OCP}–anodic polarization loop was performed five times to monitor corrosion evolution over time. Finally, an anodic polarization at a rate of 0.2 mV/s from −0.03 to +0.5 V/E_{OCP} terminated the electrochemical study of the modified substrates. The total analysis took about two days per sample. All these measurements were performed using a VSP potentiostat (BioLogic, Seyssinet-Pariset, France) controlled by the EC-Lab software (BioLogic).

2.4. Adhesion Measurement Method

Coating adhesion was investigated by scratch-test measurements using a Fischerscope ST200 tester (Helmut Fischer, Sindelfingen, Germany) equipped with a Rockwell diamond indenter (Helmut Fischer; radius of 200 µm, 90° angle). Five scratches were performed with a normal load increasing from 0 to 10 N at a 10 N/min rate. Observations coupled with the monitoring of acoustic emission and force sensors allowed us to identify the damaging mechanism of the coatings. The critical load corresponding to the complete delamination of the coating was measured.

3. Results and Discussion

3.1. Modeling of Implantation Profiles

The calculated implantation profiles of Ar, Ti and Zr using the SRIM-2013 software (Figure 1) all display Gaussian-like shapes with a tail penetrating deep into the solid. The heaviest ion, Zr, displays a narrower distribution (0–3.5 nm) than the lighter ions, Ti (0–4.0 nm) and Ar (0–4.5 nm), a mass dependence previously reported by Cano *et al.* [38]. The maximum concentration, corresponding to 10 at.% for Ti and Ar and around 12 at.% for Zr, is attained at a penetration depth of approximately 1.2 nm for Ti and Ar and up to 1.4 nm for Zr. These calculations indicate that the implantation under these conditions is performed to a very shallow depth (from 0 up to 4.5 nm) that can be even thinner under the real experimental conditions. Additionally, note that these calculations do not take into account the sputtering effect of incident ions on the substrate. These effects may alter the actual localization and profile distribution of the elements in the substrate.

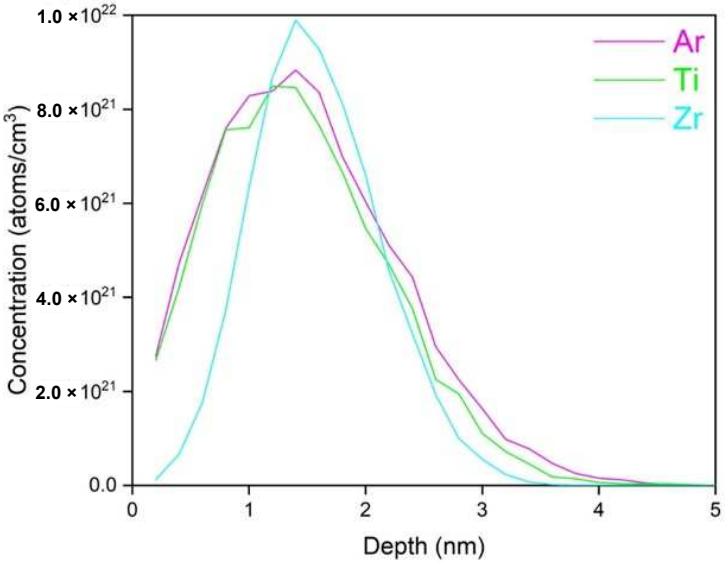


Figure 1. Concentration profiles of Ar, Ti and Zr species on 304L stainless steel calculated using SRIM 2013 versus implantation depth for 10^4 ions. Violet: Ar; green: Ti; cyan: Zr.

3.2. Structural and Chemical Analyses of Etched Coupons

GAXRD patterns for the bare 304L substrate and etched specimens are shown in Figure 2. For the initial 304L substrate, austenite (γ) and ferrite (α) phases are observed. The austenite contributions at 43.8 (111), 50.9 (200) and 74.8°2θ (220) are more intense than

the ferrite ones at 44.7 (110), 65.1 (200) and 82.3°2θ (211). The XRD peaks of all etched samples are broader compared to the initial substrate. For instance, the γ (200) contributions at 50.9°2θ for the Ar^+-, Ti^+- and Zr^+-etched samples are wider by about 6, 13 and 21%, respectively. Moreover, the amplitude of austenite (γ) contributions decreases, and that of ferrite (α) almost disappears, with only two residual contributions at 44.7 and 82.3° 2θ, after metal ion etchings (Ti^+ and Zr^+).

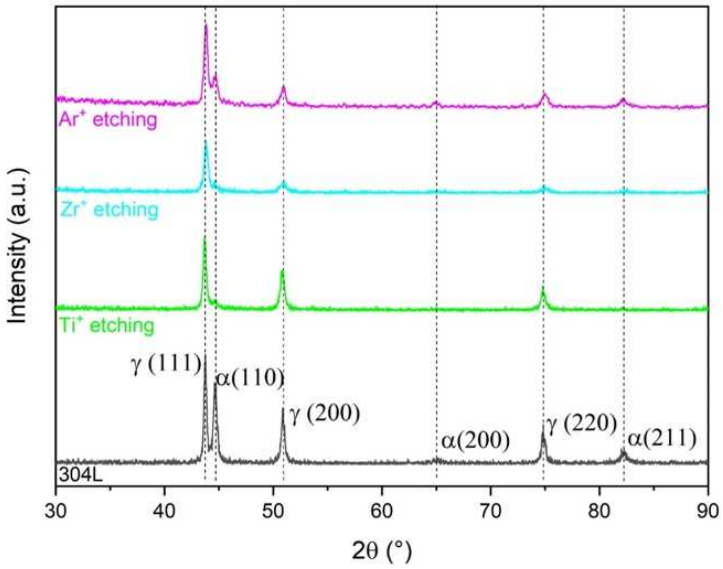


Figure 2. GAXRD patterns at 0.5° incident angle for the raw and etched (Ar^+, Zr^+ and Ti^+) 304L samples.

The three etchings do not trigger the formation of new phases, in accordance with previous results on the implantation of Ti and Ar in steels [35,36] or other elements in stainless steel [37,38]. The increase in width and decrease in the amplitude of the XRD peaks (ferrite and austenite phases) suggests amorphization after etching, as already noticed for ion implantation in stainless steel [39,40]. These observations are consistent with highly energetic incident ions creating damage and deformations in the crystalline lattice, thereby reducing crystallinity [39–42]. This amorphization seems to be stronger for the Ti^+- and Zr^+-etched samples because of the simultaneous bombardment from metal and Ar^+ ions and leads to the disappearance of surface ferrite, whereas Ar^+-etched samples undergo only Ar^+ bombardment leading only to a decrease in the presence of surface ferrite. Nonetheless, further investigation is necessary to study this amorphization in more detail.

XPS analyses were performed to study the etched surfaces. The signals from Ar, Ti and Zr were observed for these surfaces, confirming their presence as implanted ions at the extreme surface. Quantification of XPS spectra using the areas of spectrum peaks indicates that Ti (7 at.%) and Ar (5 at.%) are present after Ti^+ etching. Similarly, after Zr^+ etching, Zr (6 at.%) and Ar (6 at.%) are observed at the extreme surface of the substrate. Finally, in the case of Ar^+ etching, Ar (4 at.%) and Zr (7 at.%) are detected. The surface compositions of the Ar^+- and Zr^+-etched samples are similar to one another according to XPS analysis, whereas XRD analysis (Figure 2) suggests that the samples have a different crystalline structure. The unexpected Zr contribution observed on the Ar^+-etched sample can be attributed to resputtering effects from the vacuum chamber walls and the substrate holder.

Figure 3 reveal obvious differences between the XPS spectra for initial 304L and Ar^+-, Ti^+- or Zr^+-etched samples. For all samples, typical contributions from surface contamination, such as C, are observed (Figure 3h), as the analyses were performed without any *in situ* surface cleaning in the XPS chamber.

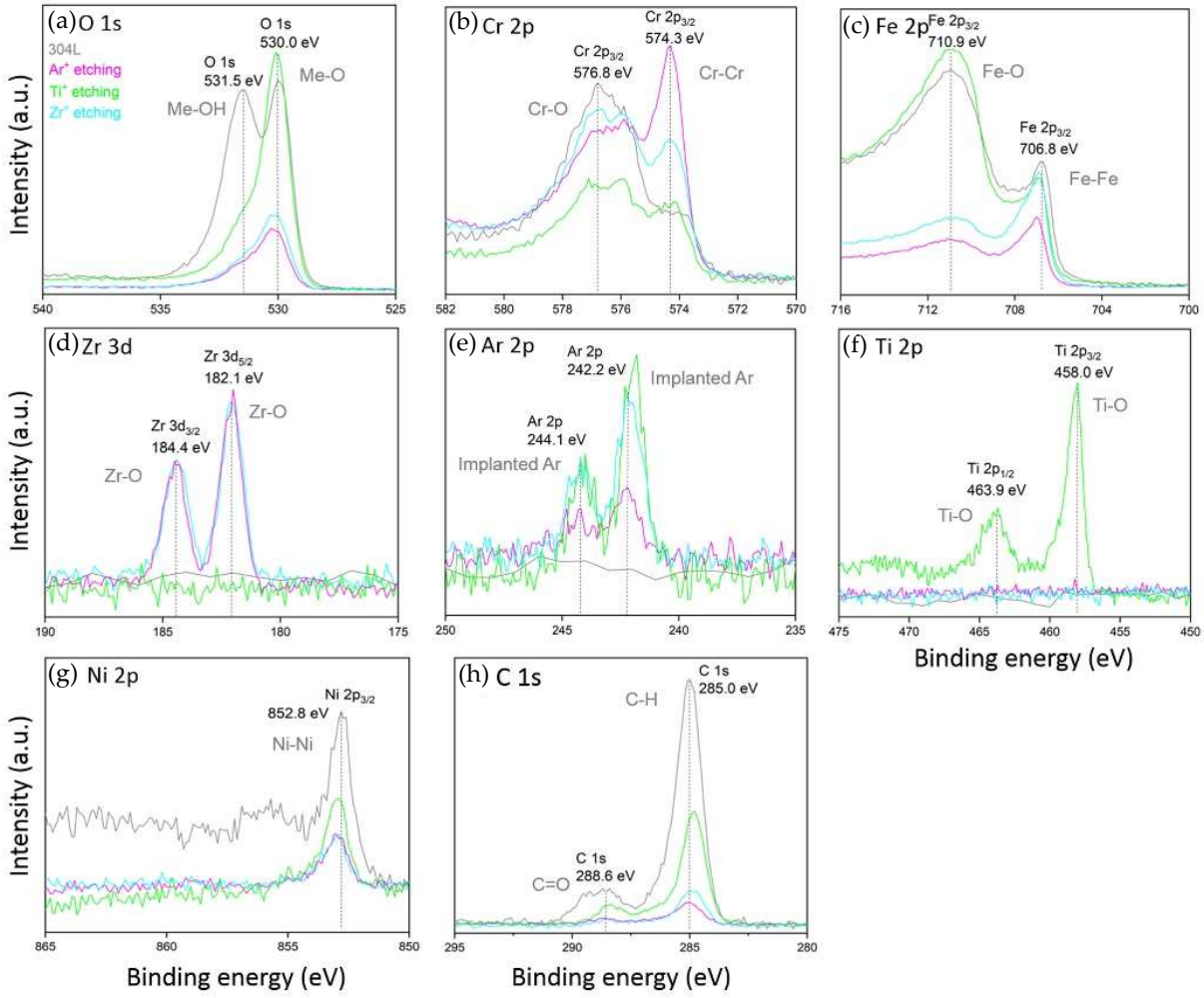


Figure 3. High-resolution XPS spectra of (**a**) O 1s, (**b**) Cr $2p_{3/2}$, (**c**) Fe $2p_{3/2}$, (**d**) Zr 3d, (**e**) Ar 2p, (**f**) Ti 2p, (**g**) Ni 2p and (**h**) C 1s of raw and etched 304L samples.

The XPS analysis of the initial 304L substrate shows the presence of metal hydroxides (Fe or Cr hydroxides at 531.5 eV for O 1s) [38] and oxides (oxides at 530.0 eV for O 1s [38], Cr_2O_3 at 576.8 eV for Cr $2p_{3/2}$ [38,41] and Fe_2O_3 at 710.9 eV for Fe $2p_{3/2}$ [38]). However, the contribution at 531.5 eV for O 1s can also be attributed to the surface contamination of the samples. Contributions at 574.3, 706.8 and 852.8 eV are attributed to metallic Cr (Figure 3b), Fe (Figure 3c) and Ni (Figure 3g), respectively [38,41,43]. The unique contribution of metallic Ni to the Ni 2p level (Figure 3g) is explained by the preferential oxidation of Fe, Cr, Zr and Ti [44,45]. These results indicate that the native passive layer formed on the 304L surface is mainly composed of Fe and Cr oxides and hydroxides, which could be consistent with the formation of a mixed Fe(III) and Cr(III) oxy-hydroxide layer reported in the literature [44–47].

Etched samples exhibit similar contributions in shape and position for each electronic level but with distinct intensities. The hydroxide contribution at 531.5 eV for O 1s decreases in amplitude and becomes a shoulder of the oxide peak at 530 eV after Ar^+, Ti^+ or Zr^+ etchings (Figure 3a). For Cr 2p, the peak assigned to the oxide state at 576.8 eV tends to decrease in intensity, especially after Ti^+ etching. On the other hand, the metal contribution at 574.3 eV increases, especially after Ar^+ and Zr^+ etchings (Figure 3b). For Fe 2p, the signal associated with the Fe oxide (Fe(III)) at 710.9 eV decreases after Ar^+ and Zr^+ etchings (Figure 3c). This decrease in intensity can indicate the decrease in the concentration of Cr(III) oxide, *i.e.*, Cr_2O_3 after Ti^+ etching and Fe_2O_3 after Ar^+ and Zr^+ etchings on the

surface oxide layer. The metal contribution is observed below the oxide layer, and its increase in intensity shows that the surface film becomes thinner [1].

Figure 3d show the Zr $3d_{3/2}$ (184.4 eV) and Zr $3d_{5/2}$ (182.1 eV) contributions attributed to Zr oxide, most likely as Zr(IV), *i.e.*, ZrO_2 [41,46], after Zr^+ and Ar^+ etchings. The Ar 2p spectrum (Figure 3e) reveals the two spin-orbit levels at 242.2 eV (Ar $2p_{3/2}$) and 244.1 eV (Ar $2p_{1/2}$), demonstrating the presence of implanted Ar [48] after all etchings. For Ti^+-etched samples, two peaks are observed on the Ti 2p spectrum (Figure 3f) at binding energies of 463.9 (Ti $2p_{1/2}$) and 458.0 eV (Ti $2p_{3/2}$) and are associated with Ti(IV), *i.e.*, TiO_2 [49–51]. There is no identified contribution from metal Ti (454.1 eV) or Zr (178.9 eV). This suggests that, in addition to Fe and Cr, Zr and Ti formed oxides on the surface, possibly upon exposition to ambient air after withdrawal from the deposition chamber [52]. Thus, Ti^+ etching leads to modification of the surface by promoting Ti oxide. A similar effect is observed for Zr^+ etching, which shows a Zr oxide. The metal ions can be incorporated into the crystal lattice as replacements [31]. This suggests a doping effect, *i.e.*, a Ti atom replaces a Cr atom in the crystal lattice as observed in [53,54] for a Cr_2O_3 lattice. The ionic radii of Ti^{4+} (60 pm) and Cr^{3+} (61 pm) are similar, leading to a negligible change in the lattice for this substitution [54]. A similar phenomenon can be observed for Zr^+ etching, where a Zr^{4+} ion could substitute for a Fe^{3+} ion present in a crystalline lattice, *e.g.*, Fe_2O_3 [55,56].

Figure 4 show the XPS depth profiles of the initial 304L substrate and the Ti^+- and Zr^+-etched samples. Depth profiles were not collected for the Ar^+-etched sample since a 1 keV Ar^+ ionic beam is used for surface erosion. The native surface layer of the initial 304L is composed of a mixture of Fe(III) and Cr(III) oxides (up to around 70 and 12 at.% at the surface, respectively, see Figure 4a). In addition, Ni enrichment is observed near the oxide/metal interface, which is due to the selective oxidation of Fe and Cr [44–46]. The oxide/metal interface seems broader after etching. Depth profiles also confirm that the amount of Fe(III) oxide decreased upon Ti^+ or Zr^+ etching (from around 70 to 62 at.% for Ti^+ and 29 at.% for Zr^+). In addition, the surface oxide film becomes thinner after the incorporation of Zr and Ti metal ions (Figure 4), as reported in [43].

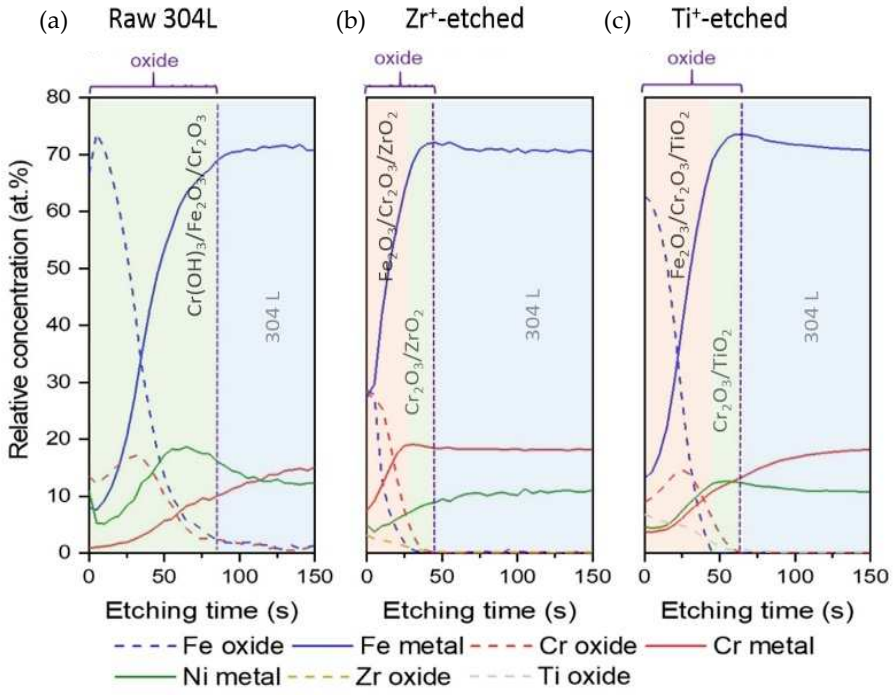


Figure 4. XPS depth profiles of (**a**) raw 304L steel and (**b**) Zr^+- and (**c**) Ti^+-etched samples.

The depth profiles also confirm the presence of oxidized Ti and Zr on the extreme surface after Ti^+ and Zr^+ etchings. However, the Ti and Zr depth profiles do not show a Gaussian shape, contrary to previous observations [43,57] and SRIM calculations (Figure 1).

The amount of Ti or Zr decreases to zero after 60 or 40 s of erosion, respectively. In contrast, the amounts of metal Fe, Cr and Ni increase along with the erosion depth and eventually reach constant values corresponding to bulk 304L.

The composition of the surface layers is superimposed on the XPS depth profiles (Figure 4). The native surface layer of the 304L steel substrate is usually described as an oxy-hydroxide film, showing a mixture of Fe(III) and Cr(III) oxides and hydroxides (Figure 4a) [44,46,47]. For the etched samples (Figure 4b,c), the hydroxide species at the extreme surface disappear according to previous XPS results (Figure 3), and a bilayer arrangement seems to be present. The outer layer is composed of mixed oxides based on Fe(III), Cr(III) and Ti(IV)/Zr(IV), and the inner layer of Ti(IV)/Zr(IV) and Cr(III) mixed oxides.

The substrate/metallic bond coat interface after metal ion etching was studied in more detail by TEM (Figure 5). For analytical reasons, a thin bond coat (200-nm-thick) was deposited after etching for both metal ion etchants. The bright-field TEM images reveal a clean and defect-free substrate/metallic bond coat interface for both samples. The TEM profiles (Figure 5c,d) also confirm the absence of contamination at the interface. In addition, no secondary or amorphous phase seems to have formed at this interface, suggesting a good adhesion between the metallic bond coat and the substrate (Figure 5a,b). The thickness of the interface, estimated from TEM observations, equals about 2 nm for the Ti-based sample and 4 nm for the Zr-based sample.

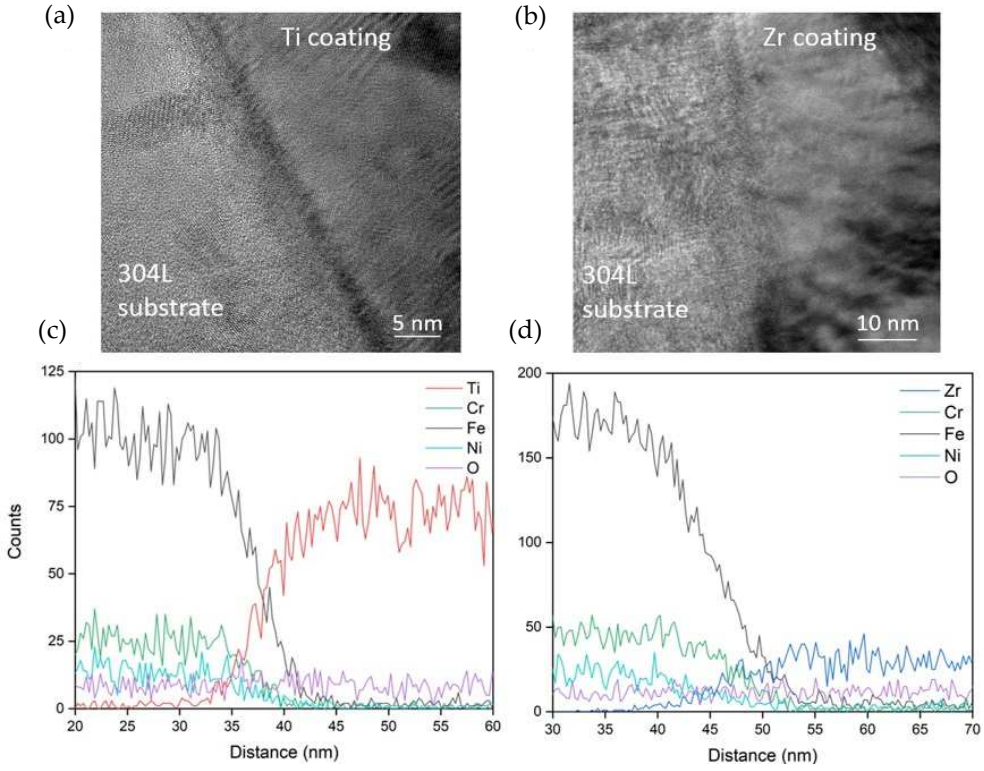


Figure 5. TEM observation of the substrate/metallic bond coat interface of (**a**) Ti^+-etched + Ti-coated and (**b**) Zr^+-etched + Zr-coated samples and TEM profiles for (**c**) Ti^+-etched + Ti-coated and (**d**) Zr^+-etched + Zr-coated samples.

In parallel, two APT analyses were performed to investigate the chemical gradients near the substrate/metallic bond coat interface and to estimate the interface thickness of the Zr^+-etched, Zr-coated sample. Figure 6a show the APT concentration profile obtained using APT equipment in electrical mode and a 3D reconstruction software that allows choosing the sampling volume. The objective is to have the best compromise between spatial resolution and counting statistics to estimate the substrate/metallic bond coat interface thickness as accurately as possible. Figure 6b show the APT concentration profile

obtained using an APT device in laser mode and the software provided by the supplier. The substrate/metallic bond coat interface is plane but slightly tilted with respect to the axis of the APT analysis. Iron and Cr are observed on the Zr metallic bond coat side of the profile (Figure 6a,b). The thickness of the substrate/metallic bond coat interface is estimated at about 2–5 nm, depending on whether the presence of Fe and Cr in the Zr bond coat is taken into account.

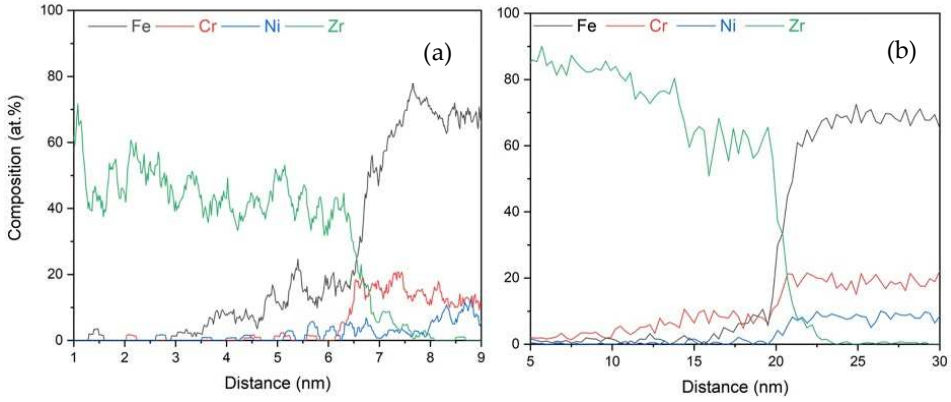


Figure 6. APT concentration profiles obtained for the Zr^+-etched and Zr-coated sample performed (**a**) in electrical mode on IRMA GPM platform and (**b**) in laser mode on CEA platform.

The detection of Fe or Cr in the APT profile for the Zr bond coat may be an artifact due to field effects during the APT analysis; TEM and XPS analyses disproved the occurrence of Fe or Cr contamination or Fe/Zr and Cr/Zr. Further investigations are required to determine the origin of this spurious signal. Moreover, no oxide layer was observed at the substrate/Zr interface by APT analyses. It is worth noticing that O is very difficult to quantify due to isotopic overlays.

In conclusion, HiPIMS etching using Ar plasma with Ti or Zr sputtering resulted in the implantation of these elements on several nm and a slight amorphization of the 304L crystal lattice. The 304L native oxide layer was found to be thinner and its composition altered, partially replacing Cr or Fe with Ti or Zr. Following etchings, the deposition of a 200 nm-thick coating generated a clean and defect-free nanometer-thick substrate/metal coating. There was no external contamination for metal-ion-etched samples, which should improve the adhesion and anticorrosive properties [27]. The effect of these surface modifications on the corrosion behavior of the 304L and the adhesion of the metallic bond coat on the substrate will now be evaluated.

3.3. Adhesion Properties of the Substrate/Metallic Bond Coat System

Five scratch-test measurements were performed on substrate/metallic bond coat systems pre-treated by Ar^+ etching, metal ion etching or not etched to study the influence of etching on the coating adhesion on the substrate. Critical load values (Lc), which correspond to coating delamination, are shown in Figure 7. The Lc value for the Ti^+-etched, Ti-coated sample is higher than for the Ar^+-etched, Ti-coated sample. The same tendency is observed for the Zr-based samples. It is worth noticing that Lc values not only depend on the etching step but also on the metal used for the metal coating. Moreover, the Zr-coated sample without pre-treatment shows the lowest Lc value of all Zr-based specimens. This demonstrates the beneficial effect of etching on substrate/metallic bond coat adhesion, as expected, probably because of the formation of a clean and defect-free interface. On the other hand, poor adhesion is observed after Ar^+ etching. This can be explained by the incorporation of Ar as interstitials in the crystal lattice, which increases the stresses and weakens the interface [31]. Thus, etching using metal ions is better as the etchants are incorporated as replacements in the crystal lattice, thus strengthening the interface [31].

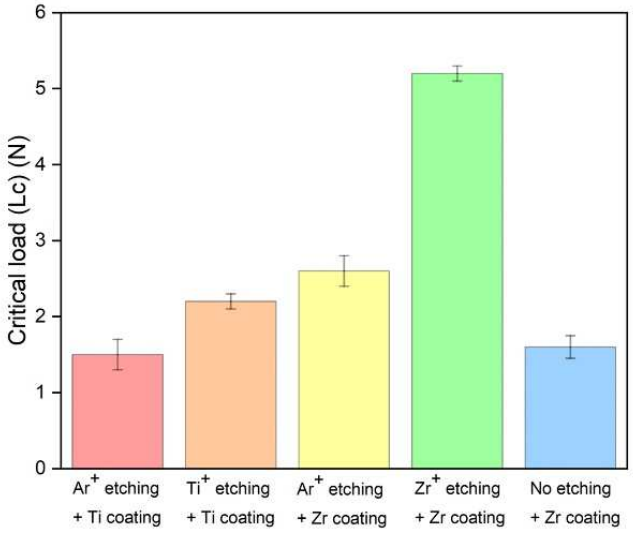


Figure 7. Average critical load value (Lc) of the substrate/metallic bond coat systems obtained from five scratch-test measurements.

3.4. Electrochemical Investigations in a Nitric Acid Environment

3.4.1. Etched Substrates

Figure 8 show the potentiodynamic polarization curves of the initial and etched substrates in a nitric acid solution at boiling temperature after 48 h of immersion. The corrosion potential (E_{corr}) and corrosion current density (J_{corr}) were derived from a Tafel extrapolation of the measured anodic polarization experiment performed to limit sample degradation (Figure 8). The E_{corr} value for the raw 304L steel equals 0.96 V/SHE after 48 h in nitric acid (Table 2). As a comparison, E_{corr} values of the etched substrates shift toward positive (nobler) values. After 48 h, E_{corr} of Ti^+-, Zr^+- and Ar^+-etched substrates stabilize around 1.07 ± 0.01 V/SHE.

Etching also affects corrosion currents. After 48 h of immersion (Figure 8), J_{corr} equals 1×10^{-4} mA/cm^2 and 9×10^{-5} mA/cm^2 for the Ti^+-etched and Zr^+-etched samples, respectively, compared to 6×10^{-4} mA/cm^2 for the initial substrate and the Ar^+-etched sample.

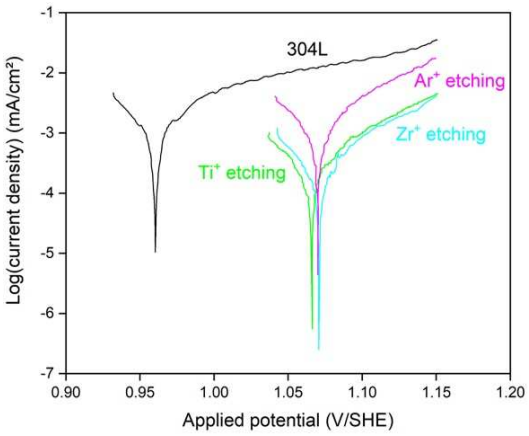


Figure 8. Potentiodynamic polarization curves of raw and etched 304L steel in a nitric acid solution at boiling temperature after 48 h of immersion. Black: initial 304L; violet: Ar^+ etching; green: Ti^+ etching; cyan: Zr^+ etching.

Table 2. Corrosion potential (E_{corr}) and current density (J_{corr}) values after 48 h of immersion in a nitric acid solution at boiling temperature.

Samples	E_{corr} (V/SHE)	J_{corr} (mA/cm^2)
304L	0.96	6×10^{-4}
Ar^+ etching	1.07	6×10^{-4}
Ti^+ etching	1.07	1×10^{-4}
Zr^+ etching	1.07	9×10^{-5}

All etching treatments have a positive effect on the electrochemical behavior of the 304L steel in nitric acid, but this effect is more pronounced for metal ion (Ti^+ and Zr^+) etchants than for Ar^+. This can be explained by the reduction of the ferrite content and amorphization of the surface upon HiPIMS etching. Prasad Rao *et al.* showed that ferrite could be preferentially attacked in nitric acid environments [58]. In addition, the passive film is more protective at the surface of austenite compared to ferrite [44,59]. Therefore, decreasing the amount of ferrite can improve the corrosion resistance of the steel. Additionally, potentiodynamic polarization curves of Ti^+- and Zr^+-etched samples reveal ennoblement, which can indicate an increase in the corrosion potential due to ion implantation [60] and modification of the passive layer. In fact, the incorporation of Ti and Zr induces the formation of Ti and Zr oxides on the surface, which can reinforce the passive layer (Figure 4) and decrease the oxidation rate of 304L steel due to their stability in nitric acid environments. The higher nobleness of these etched surfaces can also be explained by the presence of a smaller amount of ferrite, which is known to be less noble than austenite [59]. Moreover, a reduced corrosion current after 48 h of immersion in boiling nitric acid is observed for these etchings. Better corrosion resistance is generally observed when the corrosion potential is higher, and the corrosion current density is decreased, leading to a lower corrosion rate [61,62]. Consequently, the results hint at better corrosion resistance owing to structural modifications of the 304L surface and/or modification of the passive layer due to ion etching.

3.4.2. Etched and Metallic Bond Coat Deposited 304L Substrates

Figure 9 show the potentiodynamic polarization curves of initial 304L and etched, metallic bond coat-deposited substrates in a nitric acid solution at boiling temperature after 6 h of immersion. Table 3 show that the E_{corr} value for the initial 304L equals 0.98 V/SHE after 6 h of immersion. In comparison, a dispersion of E_{corr} values for the etched, metallic bond coat-deposited samples is observed. Only E_{corr} of Ar^+-etched and Zr-coated, Zr-coated samples are shifted toward positive values (1.02 and 1.03 V/SHE, respectively).

The effect of coatings is more visible on corrosion currents. After 6 h of immersion, J_{corr} decreases by an order of magnitude for all the etched, metallic bond coat-deposited samples down to 10^{-4} mA/cm^2 and even to about 10^{-5} mA/cm^2 for the Zr^+-etched, Zr-coated sample, compared to 1×10^{-3} mA/cm^2 for raw 304L steel.

Etching followed by metallic bond coat deposition has a positive effect on the electrochemical behavior of the 304L steel in a nitric acid environment. Nonetheless, this effect is more pronounced for the Zr^+-etched, Zr-coated sample than for the other ones, showing that the beneficial effect of Zr^+ etching compared to the Ar^+ one is still observed after the deposition of the bond coat. This confirms that the substrate/metallic bond coat interface is formed differently depending on the etchant type (Zr^+ or Ar^+). The better corrosion resistance of the Zr^+-etched, Zr-coated sample is correlated with the higher adhesion observed for this sample (shown in Section 2.3). A higher adhesion may induce better protection of the coating in an aggressive environment by preventing the electrolyte from reaching the substrate. Moreover, Zr is more resistant than Ti in a nitric acid environment due to the formation of a dense and insulating oxide layer (ZrO_2) on its surface [63].

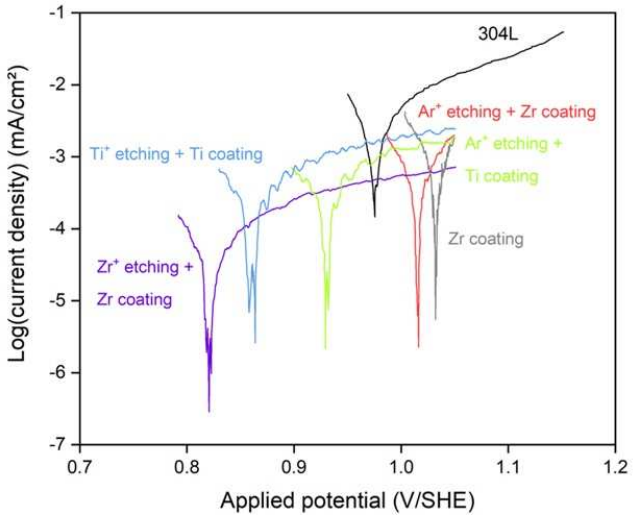


Figure 9. Potentiodynamic polarization curves of raw 304L and etched and metallic bond coat deposited samples in a nitric acid solution at boiling temperature after 6 h of immersion. Black: initial 304L; light green: Ar^+ etching + Ti coating; red: Ar^+ etching + Zr coating. Light blue: Ti^+ etching + Ti coating; deep blue: Zr^+ etching + Zr coating; grey: Zr coating.

Table 3. Corrosion potential (E_{corr}) and current density (J_{corr}) values after 6 h of immersion in a nitric acid solution at boiling temperature.

Samples	E_{corr} (V/SHE)	J_{corr} (mA/cm^2)
304L	0.98	1×10^{-3}
Ar^+ etching + Ti coating	0.93	1×10^{-4}
Ti^+ etching + Ti coating	0.86	1×10^{-4}
Ar^+ etching + Zr coating	1.02	1×10^{-4}
Zr^+ etching + Zr coating	0.82	2×10^{-5}
Zr coating	1.03	3×10^{-4}

3.4.3. Characterization of the Electrochemically Investigated Surface

XPS spectra of the main electronic levels of the initial 304L and etched samples are shown in Figure 10. The O 1s spectra display large bands containing the two contributions of metal hydroxides and metal oxides at 531.6 and 530.7 eV, respectively (Figure 10a) [37]. Moreover, one main Cr 2p peak at 576.8 eV associated with Cr oxide (Cr_2O_3) and a minor peak at 574.4 eV, which is characteristic of Cr metallic binding [38,39], are observed for all samples (Figure 10b). The Fe 2p spectra (Figure 10c) display the same two peaks at 711.4 eV (Fe oxide) and 706.9 eV (Fe metal) observed before electrochemical investigations of the etched samples [37]. The contribution at 852.9 eV is attributed to metallic Ni (Figure 10g), as previously observed (Figure 3g). In addition, the contributions from surface contamination, mainly C, are still observed after immersion in nitric acid but differ depending on the sample (Figure 10h).

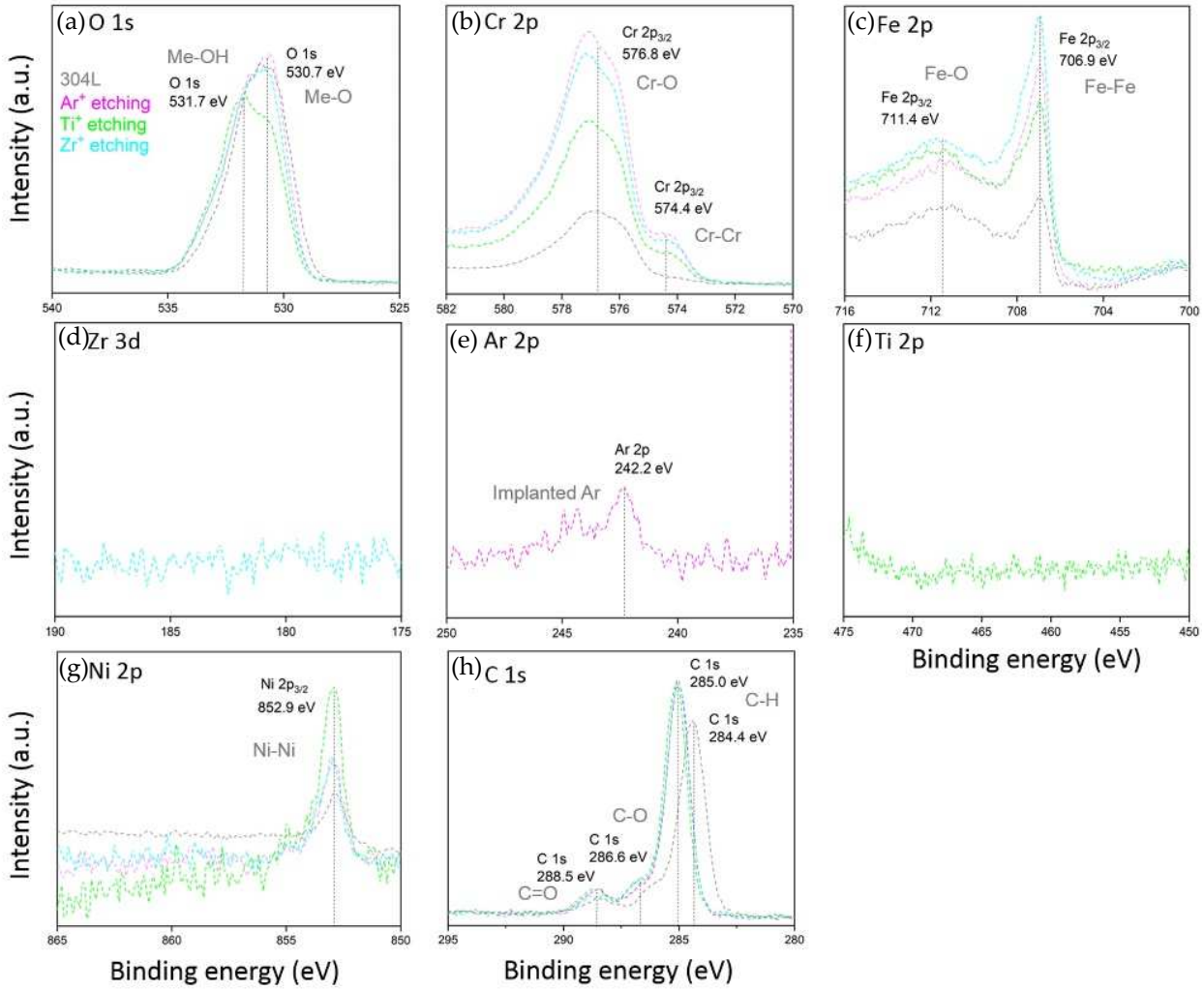


Figure 10. High-resolution XPS spectra of (**a**) O 1s, (**b**) Cr $2p_{3/2}$, (**c**) Fe $2p_{3/2}$, (**d**) Zr 3d, (**e**) Ar 2p, (**f**) Ti 2p, (**g**) Ni 2p and (**h**) C 1s of raw and etched 304L steel after 48 h in nitric acid solution at boiling temperature.

After electrochemical measurements, metal Ti and Zr are no longer detected by XPS (Figure 10d,f), whereas the spectrum for the Ar^+-etched sample still exhibits a residual Ar contribution at 242.2 eV (Figure 10e). The absence of Ti and Zr detection suggests that these elements have actually dissolved in the electrolyte. The presence of Ar at the surface after 48 h of reaction can be explained by the different behavior of Ar compared to Ti and Zr, which does not combine with the other surface elements and cannot oxidize.

The XPS depth profiles were measured on the 304L steel and etched samples after electrochemical measurements (Figure 11). These measurements show that metal Ti and Zr contents significantly decreased at the extreme surface, down to, respectively, 0.9 and 0.4 at.% after electrochemical tests compared to 7 and 6 at.% before the immersion in nitric acid. Moreover, distinct XPS depth profiles were obtained for initial 304L and Zr^+- and Ti^+-etched samples. The profile of the initial 304L shows a higher oxygen penetration and no clear oxide/metal interface compared to the etched samples. In addition, the Ni enrichment observed near the oxide/metal interface is greater for etched samples (Figure 11b,c) than for the initial 304L due to the selective oxidation of Fe and Cr at the extreme surface. The metal ion etching induces a decrease in the thickness of the passive oxide film. The passive layer formed in nitric acid is made of a mixture of Fe and Cr oxides as the initial layer. However, the amount of Fe oxide seems to be the same in the extreme surface for all samples (around 10 at.% for initial 304L steel and Ti^+-etched, and 9 at.% for Zr^+-etched) and lower than

in the initial layer (around 70 at.% for initial 304L, 62 at.% for Ti^+-etched and 29 at.% for Zr^+-etched). On the other hand, the amount of Cr oxide is slightly different between 304L steel and the etched samples (around 66 at.% for initial 304L, 54 at.% for Ti^+-etched and 53 at.% for Zr^+-etched), but it is very high compared to the initial film (around 13 at.% for initial 304L steel, 9 at.% for Ti^+-etched and 29 at.% for Zr^+-etched). The presence of this Cr-enriched passive layer is explained by the preferential dissolution of iron during passivation [44,64].

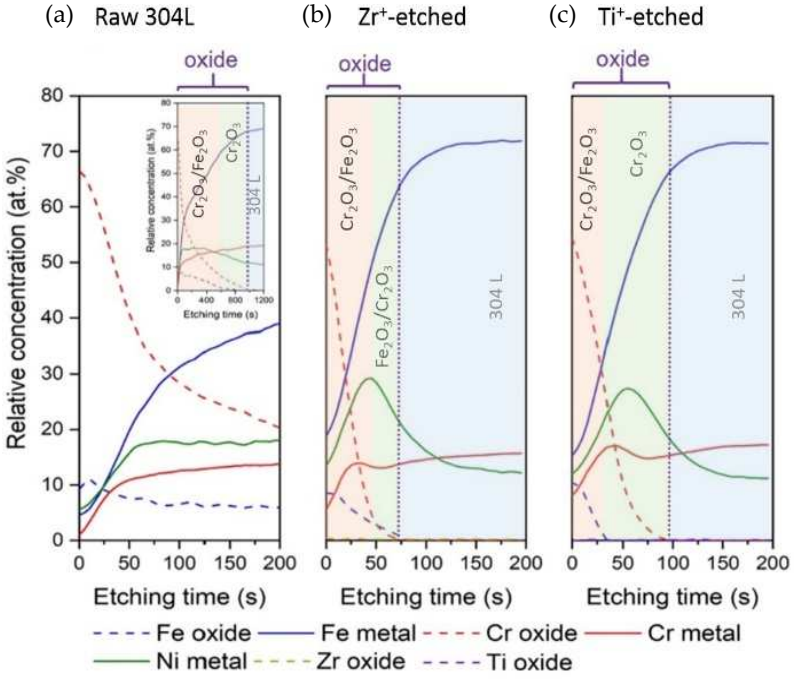


Figure 11. XPS depth profiles of (**a**) raw 304L steel and (**b**) Zr^+- and (**c**) Ti^+-etched samples after 48 h of immersion in nitric acid solution at boiling temperature.

Ti and Zr almost disappeared from the sample surface after electrochemical tests, suggesting that their initial amounts may not have been sufficient to form a perennial Ti or Zr oxide layer. However, the etching effect on the crystalline structure, *i.e.*, a decrease in the ferrite phase, could explain the decrease in the corrosion rate by preventing a possible galvanic coupling between the austenite and ferrite phases. Another hypothesis is that Ti and Zr, even in small amounts, could densify and reinforce the passive layer. Therefore, this would increase the corrosion resistance properties despite the passive film thinning compared to the 304L steel.

The composition of the passive films formed after electrochemical measurements in nitric acid is superimposed on the XPS depth profiles in Figure 11. The passive film shows a bilayer structure. The outer layer is mostly made of a mixture of Cr and Fe oxides for all the samples. In contrast, the inner layer differs according to the sample under study: Cr oxide predominates for 304L steel and Ti^+-etched sample, and a mixed Fe and Cr oxide is observed for the Zr^+-etched sample.

To summarize, the combination of electrochemical results and subsequent XPS analysis indicates that the impact of Ar^+ etching (inert gas) is distinct from that of Ti^+ and Zr^+ etchings (metal ions): Ar incorporation seems to slightly improve the corrosion resistance of the 304L steel. The Ar^+ etching induces only small changes in the 304L crystalline structure, in contrast to metal ion etching. A similar effect was observed for the implantation of another inert gas (Ne) on 304L steel and was related to the creation of a high density of dislocations in the crystalline structure [65]. On the other hand, the metal ion etching induces an extended modification of the crystalline structure and leads to the formation

of a modified and probably denser passive layer compared to initial 304L steel. This may explain their better corrosion resistance in a nitric acid environment.

Focus is now placed on the Zr^+-etched, Zr-coated sample as it offers the best corrosion resistance properties according to the previous electrochemical measurements. Figure 12 show the XPS depth profiles of this sample before and after electrochemical measurements in nitric acid. These measurements indicate that a Zr-based oxide layer is present at the extreme surface of the Zr coating before immersion in nitric acid. Figure 12b show that this oxide film is present over a longer XPS erosion time after 48 h of immersion in nitric acid, indicating that its thickness has increased.

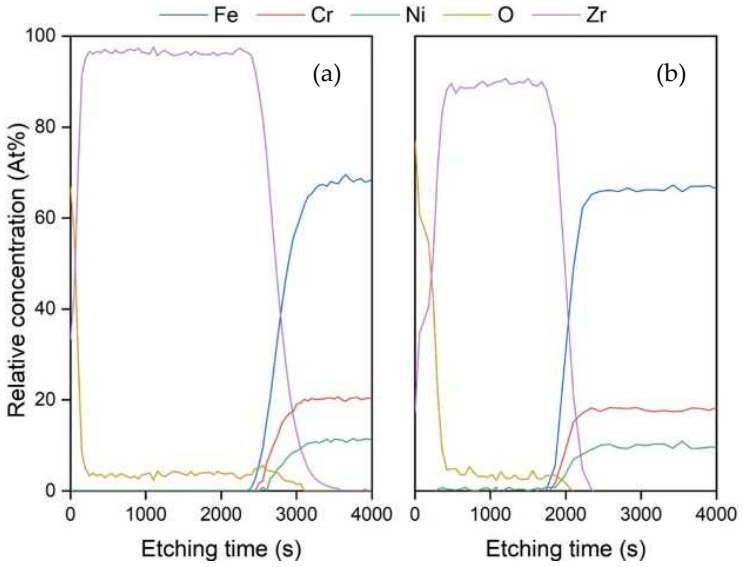


Figure 12. XPS depth profiles of Zr^+-etched and Zr-coated sample (**a**) before and (**b**) after 48 h of immersion in nitric acid solution at boiling temperature.

The oxide layer present before electrochemical measurements probably formed when the samples were removed from the vacuum chamber due to the high affinity of Zr for oxygen. This oxide film is not modified during the nitric acid immersion, unlike the initial layer observed on the etched samples (Section 2.2). This is due to the high amount of Zr, which allows the Zr oxide layer to grow during the immersion in nitric acid. Further analysis is planned to establish whether this oxide layer grows with immersion time or if there is a dissolution of this film.

4. Conclusions

This work assessed with extended spatial resolution and structural detail the effect of 304L stainless steel etching using ionized vapors of Ar, Ti (Ar and Ti) and Zr (Ar and Zr) generated by HiPIMS. This ion etching pre-treatment results in the surface modification of 304L steel by implantation of the sputtered elements. Additionally, etchings do not trigger the crystallization of new phases that could be detected by XRD but reduce the ferrite content and amorphize the 304L surface. The incorporation of ions (around 6–7 at.%) alters the substrate extreme surface by modifying the nature and proportion of native oxides, partially replacing Fe and Cr oxides with Ti and Zr ones and limiting the possible consequences of a chemically sharp interface. The substrate/metal coating interface formed after etching is free of external contamination and is about 1 nm- thick, as seen in TEM and APT. In addition, HiPIMS metal ion etching shows superior substrate/metal coating adhesion compared to inert gas etching. This definitively demonstrates the superior performance of metal ion etching compared to Ar for the elaboration of strong metal-coatings interfaces for industrial applications.

The change in the composition of the metal-etched surface enhances the formation of oxidized (noble) surfaces when exposed to air. These surfaces may improve resistance to corrosion, should they be accidentally exposed (*e.g.*, after coating scratching). Evaluation of corrosion behavior in a boiling nitric acid solution indicates an increase in the corrosion potential and a decrease in the corrosion current density for Ti^+- and Zr^+-etched surfaces after 48 h of immersion. In contrast, no long-term improvement is observed for the Ar^+-etched surface due to the small changes in the crystalline structure. On the other hand, HiPIMS metallic etching decreases the corrosion rate of the 304L substrate by forming a more protective and dense passive layer, which hinders the charge transfer process.

Collectively, these results confirm that the HiPIMS metal ion etching pre-treatment modifies the substrate/coating interface, which can be beneficial for the long-term performance of the coatings. Moreover, these modifications will provide additional protection in areas where coatings may fail. After the deposition of a 200 nm-thick metal coating, this beneficial effect is observed only for Zr^+ etching in the nitric acid solution. Further investigation may be performed to improve these anti-corrosion properties, *e.g.*, by tweaking the chemical composition, incident flux and energy of the etching ions. It also opens the door to similar investigations on specific alloys, and aggressive environments, in order to optimize the process-function relationship. Finally, this work emphasized the importance of mastering the etching step to elaborate an architectured coating system, *i.e.*, composed of several successive layers (metallic bond coat, oxide and metal coatings).

Author Contributions: A.C.: Methodology, Investigation, Validation, Visualization, Writing—original draft. A.M.: Supervision, Validation, Visualization, Writing—review and editing. M.L.S.: Supervision, Validation, Visualization, Writing—review and editing. D.C.G.: Writing—review and editing. B.P.: Supervision, Validation, Visualization, Writing—review and editing. F.M.: Investigation, Validation, Writing—review and editing. F.S.: Supervision, Funding acquisition, Project administration, Writing—review and editing. H.M.: Project administration, Resources. C.P.: Investigation, Validation, Writing—review and editing. E.C.: Investigation. G.B.: Investigation, Validation, Writing—review and editing. V.C.-C.: Investigation. S.N.: Supervision, Project administration. B.Y.: Investigation, Validation. Z.D.: Supervision, Funding acquisition, Project administration, Writing—review and editing. F.B.-C.: Supervision, Validation, Writing—review and editing. All authors have read and agreed to the published version of the manuscript.

Funding: This work was funded by the CEA Cross-Cutting Program on Materials and Processes Skills and by the NTU Tier1 project "Nanostructured titania with tunable hydrophilic/hydrophobic behaviour and photocatalytic function for marine structure applications" in the frame of an agreement between Sorbonne University, France and NTU, Singapore. Finally, the authors acknowledge financial support from the CNRS-CEA "METSA" French network (FR CNRS 3507) on the platform IRMA GPM.

Institutional Review Board Statement: Not applicable.

Informed Consent Statement: Not applicable.

Data Availability Statement: The data are not freely available at this time.

Acknowledgments: The authors want to acknowledge C. Cabet and M. Loyer-Prost for their contribution to SRIM calculation training and data analysis. The authors would like to acknowledge the Facility for Analysis, Characterisation, Testing and Simulation, Nanyang Technological University, Singapore, for the use of their electron microscopy/X-ray facilities and especially L. Xi and B. Yao for their contribution to TEM samples preparation and TEM analyses.

Conflicts of Interest: The authors declare no conflict of interest.

References

1. Tcharkhtchi-Gillard, E.; Benoit, M.; Clavier, P.; Gwinner, B.; Miserque, F.; Vivier, V. Kinetics of the oxidation of stainless steel in hot and concentrated nitric acid in the passive and transpassive domains. *Corros. Sci.* **2016**, *107*, 182–192. [CrossRef]
2. Féron, D. Overview of nuclear materials and nuclear corrosion science and engineering. In *Nuclear Corrosion Science and Engineering*; Elsevier Inc.: Amsterdam, The Netherlands, 2012; pp. 31–56. ISBN 9781845697655.
3. Fauvet, P. 19—Corrosion issues in nuclear fuel reprocessing plants. In *Nuclear Corrosion Science and Engineering*; Féron, D., Ed.; Woodhead Publishing: Cambridge, UK, 2012; pp. 679–728.

4. Kazazi, M.; Haghighi, M.; Yarali, D.; Zaynolabedini, M.H. Improving Corrosion Resistance of 316L Austenitic Stainless Steel Using ZrO_2 Sol-Gel Coating in Nitric Acid Solution. *J. Mater. Eng. Perform.* **2018**, *27*, 1093–1102. [CrossRef]
5. Ningshen, S.; Mudali, U.K.; Krishnan, R.; Raj, B. Corrosion behavior of Zr-based metallic glass coating on type 304L stainless steel by pulsed laser deposition method. *Surf. Coat. Technol.* **2011**, *205*, 3961–3966. [CrossRef]
6. Padhy, N.; Kamal, S.; Chandra, R.; Mudali, U.K.; Raj, B. Corrosion performance of TiO_2 coated type 304L stainless steel in nitric acid medium. *Surf. Coat. Technol.* **2010**, *204*, 2782–2788. [CrossRef]
7. Padhy, N.; Mudali, U.K.; Chawla, V.; Chandra, R.; Raj, B. Corrosion behaviour of single (Ti) and duplex (Ti–TiO_2) coating on 304L stainless steel in nitric acid medium. *Mater. Chem. Phys.* **2011**, *130*, 962–972. [CrossRef]
8. Li, C.; Chen, W.; Jiang, Q.; Wang, L.; Luo, D. Corrosion resistance of Ti-based metallic glass coating in concentrated nitric acid. *Mater. Chem. Phys.* **2014**, *143*, 900–903. [CrossRef]
9. Bensaha, R.; Bensouyad, H. *Synthesis, Characterization and Properties of Zirconium Oxide (ZrO_2)-Doped Titanium Oxide (TiO_2) Thin Films Obtained via Sol-Gel Process*; Books on Demand: Norderstedt, Germany, 2012. [CrossRef]
10. Nouri, E.; Shahmiri, M.; Rezaie, H.R.; Talayian, F. Investigation of structural evolution and electrochemical behaviour of zirconia thin films on the 316L stainless steel substrate formed via sol–gel process. *Surf. Coat. Technol.* **2011**, *205*, 5109–5115. [CrossRef]
11. Holgado, J.; Pérez-Sánchez, M.; Yubero, F.; Espinos, J.P.; González-Elipe, A. Corrosion resistant ZrO_2 thin films prepared at room temperature by ion beam induced chemical vapour deposition. *Surf. Coat. Technol.* **2002**, *151–152*, 449–453. [CrossRef]
12. Cubillos, G.I.; Olaya, J.J.; Bethencourt, M.; Cifredo, G.; Blanco, G. Resistance to Corrosion of Zirconia Coatings Deposited by Spray Pyrolysis in Nitrided Steel. *J. Therm. Spray Technol.* **2013**, *22*, 1242–1252. [CrossRef]
13. Kotoka, R.; Yarmolenko, S.; Pai, D.; Sankar, J. Corrosion Behavior of Reactive Sputtered Al_2O_3 and ZrO_2 Thin Films on Mg Disk Immersed in Saline Solution. *J. Mater. Sci. Technol.* **2015**, *31*, 873–880. [CrossRef]
14. Kaliaraj, G.S.; Vishwakarma, V.; Kirubaharan, K.; Dharini, T.; Ramachandran, D.; Muthaiah, B. Corrosion and biocompatibility behaviour of zirconia coating by EBPVD for biomedical applications. *Surf. Coat. Technol.* **2018**, *334*, 336–343. [CrossRef]
15. Shajudheen, V.M.; Rani, K.A.; Kumar, V.S.; Maheswari, A.U.; Sivakumar, M.; Kumar, S.S. Comparison of Anticorrosion Studies of Titanium Dioxide and Nickel Oxide Thin Films Fabricated by Spray Coating Technique. *Mater. Today Proc.* **2018**, *5*, 8889–8898. [CrossRef]
16. Lanzutti, A.; Lekka, M.; De Leitenburg, C.; Fedrizzi, L. Effect of pulse current on wear behaviour of Ni matrix micro- and nano-SiC composite coatings at room and elevated temperature. *Tribol. Int.* **2019**, *132*, 50–61. [CrossRef]
17. Tseluikin, V.N.; Koreshkova, A.A. Deposition of zinc–carbon nanotube composite coatings in the pulse-reverse mode. *Russ. J. Appl. Chem.* **2014**, *87*, 1251–1253. [CrossRef]
18. Tseluikin, V.; Vasilenko, E.A. Electrodeposition and properties of composite coatings based on nickel. *Russ. J. Appl. Chem.* **2011**, *84*, 2005–2007. [CrossRef]
19. Portinha, A.; Teixeira, V.; Carneiro, J.; Costa, M.F.; Barradas, N.P.; Sequeira, A.D. Stabilization of ZrO_2 PVD coatings with Gd_2O_3. *Surf. Coat. Technol.* **2004**, *188–189*, 107–115. [CrossRef]
20. Kouznetsov, V.; Macák, K.; Schneider, J.M.; Helmersson, U.; Petrov, I. A novel pulsed magnetron sputter technique utilizing very high target power densities. *Surf. Coat. Technol.* **1999**, *122*, 290–293. [CrossRef]
21. Böhlmark, J.; Helmersson, U.; Anders, A. *Fundamentals of High Power Impulse Magnetron Sputtering*; Institutionen för Fysik, Kemi och Biologi, Linköping University: Linköping, Sweden, 2006.
22. Anders, A. Tutorial: Reactive high power impulse magnetron sputtering (R-HiPIMS). *J. Appl. Phys.* **2017**, *121*, 171101. [CrossRef]
23. Alami, J.; Bolz, S.; Sarakinos, K. High power pulsed magnetron sputtering: Fundamentals and applications. *J. Alloys Compd.* **2009**, *483*, 530–534. [CrossRef]
24. Moll, E. Physical Vapor Deposition Techniques II: Ion Plating, Arc Deposition and Ion Beam Deposition. In *Advanced Techniques for Surface Engineering*; Gissler, W., Jehn, H.A., Eds.; Springer: Dordrecht, The Netherlands, 1992; pp. 181–197.
25. Ehiasarian, A.P. High-power impulse magnetron sputtering and its applications. *Pure Appl. Chem.* **2010**, *82*, 1247–1258. [CrossRef]
26. Ougier, M.; Michau, A.; Schuster, F.; Maskrot, H.; Schlegel, M.L. Effects of HiPIMS discharges and annealing on Cr-Al-C thin films. *Surf. Coat. Technol.* **2020**, *399*, 126141. [CrossRef]
27. Reinhard, C.; Ehiasarian, A.; Hovsepian, P. CrN/NbN superlattice structured coatings with enhanced corrosion resistance achieved by high power impulse magnetron sputtering interface pre-treatment. *Thin Solid Films* **2007**, *515*, 3685–3692. [CrossRef]
28. Wang, Q.-Y.; Xi, Y.-C.; Liu, X.-Y.; Liu, S.; Bai, S.-L.; Liu, Z.-D. Microstructure and mechanical properties of interface between laser cladded Hastelloy coating and steel substrate. *Trans. Nonferrous Met. Soc. China* **2017**, *27*, 733–740. [CrossRef]
29. Sarakinos, K.; Alami, J.; Konstantinidis, S. High power pulsed magnetron sputtering: A review on scientific and engineering state of the art. *Surf. Coat. Technol.* **2010**, *204*, 1661–1684. [CrossRef]
30. Santiago, J.; Fernández-Martínez, I.; Wennberg, A.; Molina-Aldareguia, J.; Castillo-Rodríguez, M.; Rojas, T.; Sánchez-López, J.; González, M.; García-Martín, J.; Li, H.; et al. Adhesion enhancement of DLC hard coatings by HiPIMS metal ion etching pretreatment. *Surf. Coat. Technol.* **2018**, *349*, 787–796. [CrossRef]
31. Ehiasarian, A.P.; Wen, J.G.; Petrov, I. Interface microstructure engineering by high power impulse magnetron sputtering for the enhancement of adhesion. *J. Appl. Phys.* **2007**, *101*, 054301. [CrossRef]
32. Karimi, M.V.; Sinha, S.; Kothari, D.; Khanna, A.; Tyagi, A. Effect of ion implantation on corrosion resistance and high temperature oxidation resistance of Ti deposited 316 stainless steel. *Surf. Coat. Technol.* **2002**, *158–159*, 609–614. [CrossRef]

33. Bakoglidis, K.; Schmidt, S.; Greczynski, G.; Hultman, L. Improved adhesion of carbon nitride coatings on steel substrates using metal HiPIMS pretreatments. *Surf. Coat. Technol.* **2016**, *302*, 454–462. [CrossRef]
34. Asri, R.I.M.; Harun, W.S.W.; Samykano, M.; Lah, N.A.C.; Ghani, S.A.C.; Tarlochan, F.; Raza, M.R. Corrosion and surface modification on biocompatible metals: A review. *Mater. Sci. Eng. C* **2017**, *77*, 1261–1274. [CrossRef]
35. Ziegler, J.F.; Ziegler, M.D.; Biersack, J.P. SRIM—The stopping and range of ions in matter (2010). *Nucl. Instrum. Methods B* **2010**, *268*, 1818–1823. [CrossRef]
36. The Stopping Power and Range of Ions in Matter (SRIM Code, Version 2013). Available online: http://www.srim.org (accessed on 5 January 2019).
37. Gudmundsson, J.T. Physics and technology of magnetron sputtering discharges. *Plasma Sources Sci. Technol.* **2020**, *29*, 113001. [CrossRef]
38. Cano, E.; Martinez, L.; Simancas, J.; Perez-Trujillo, F.J.; Gomez, C.; Bastidas, J.M. Influence of N, Ar and Si ion implantation on the passive layer and corrosion behaviour of AISI 304 and 430 stainless steels. *Surf. Coat. Technol.* **2006**, *200*, 5123–5131. [CrossRef]
39. Dudognon, J.; Vayer, M.; Pineau, A.; Erre, R. Mo and Ag ion implantation in austenitic, ferritic and duplex stainless steels: A comparative study. *Surf. Coat. Technol.* **2008**, *203*, 180–185. [CrossRef]
40. Qiu, Z.; Wang, F.; Li, Q.; Zheng, L.; Zhang, F.; Zhang, H. Corrosion and mechanical properties for Cr-coated CSS-42L bearing steel after Ti and C ions co-implantation. *Appl. Surf. Sci.* **2020**, *509*, 145293. [CrossRef]
41. Martínez, L.; Gómez, C.; Perez, F.J. Sinergistic effect of ion implantation as a surface modification technique to improve localised corrosion of AISI 304 austenitic stainless steel. *Surf. Coat. Technol.* **2005**, *195*, 70–80. [CrossRef]
42. Chang, G.; Son, J.; Kim, S.; Chae, K.; Whang, C.; Menthe, E.; Rie, K.-T.; Lee, Y. Electronic structures and nitride formation on ion-implanted AISI 304L austenitic stainless steel. *Surf. Coat. Technol.* **1999**, *112*, 291–294. [CrossRef]
43. Pelletier, H.; Mille, P.; Cornet, A.; Grob, J.; Stoquert, J.; Muller, D. Effects of high energy nitrogen implantation on stainless steel microstructure. *Nucl. Instrum. Methods Phys. Res. Sect. B Beam Interact. Mater. Atoms* **1999**, *148*, 824–829. [CrossRef]
44. Feng, K.; Wang, Y.; Li, Z.; Chu, P. Characterization of carbon ion implantation induced graded microstructure and phase transformation in stainless steel. *Mater. Charact.* **2015**, *106*, 11–19. [CrossRef]
45. Gardin, E.; Zanna, S.; Seyeux, A.; Allion-Maurer, A.; Marcus, P. XPS and ToF-SIMS characterization of the surface oxides on lean duplex stainless steel—Global and local approaches. *Corros. Sci.* **2019**, *155*, 121–133. [CrossRef]
46. Olsson, C.; Landolt, D. Passive films on stainless steels—Chemistry, structure and growth. *Electrochim. Acta* **2003**, *48*, 1093–1104. [CrossRef]
47. Maurice, V.; Yang, W.P.; Marcus, P. X-ray Photoelectron Spectroscopy and Scanning Tunneling Microscopy Study of Passive Films Formed on (100) Fe-18Cr-13Ni Single-Crystal Surfaces. *J. Electrochem. Soc.* **1998**, *145*, 909–920. [CrossRef]
48. Crist, B.V. Argon Implanted into Graphite, by XPS. *Surf. Sci. Spectra* **1992**, *1*, 376–380. [CrossRef]
49. Peng, D.; Bai, X.; Pan, F.; Sun, H.; Chen, B. Influence of titanium ion implantation on the corrosion behavior of zircalloy-4 in 1M H_2SO_4. *Mater. Chem. Phys.* **2005**, *92*, 443–447. [CrossRef]
50. Lee, H.; Lee, S.; Ada, E.; Kim, B.; Weiss, M.; Perry, S.; Rabalais, J. Shallow implantation of Ti^+ ions in sapphire [α-Al_2O_3(0001)]. *Nucl. Instrum. Methods Phys. Res. Sect. B Beam Interact. Mater. Atoms* **1999**, *157*, 226–232. [CrossRef]
51. Liu, C.; Xin, Y.; Tian, X.; Zhao, J.; Chu, P.K. Corrosion resistance of titanium ion implanted AZ91 magnesium alloy. *J. Vac. Sci. Technol. A Vac. Surf. Film.* **2007**, *25*, 334–339. [CrossRef]
52. Arenas, M.; García, I.; de Damborenea, J. X-ray photoelectron spectroscopy study of the corrosion behaviour of galvanised steel implanted with rare earths. *Corros. Sci.* **2004**, *46*, 1033–1049. [CrossRef]
53. Maldonado, F.; Novillo, C.; Stashans, A. Ab initio calculation of chromium oxide containing Ti dopant. *Chem. Phys.* **2012**, *393*, 148–152. [CrossRef]
54. Kaspar, T.C.; Sushko, P.; Bowden, M.E.; Heald, S.M.; Papadogianni, A.; Tschammer, C.; Bierwagen, O.; Chambers, S.A. Defect compensation by Cr vacancies and oxygen interstitials in Ti^{4+}-doped Cr_2O_3 epitaxial thin films. *Phys. Rev. B* **2016**, *94*, 155409. [CrossRef]
55. Wang, D.; Jin, L.; Li, Y.; Hu, H. Partial oxidation of vacuum residue over Al and Zr-doped α-Fe_2O_3 catalysts. *Fuel* **2017**, *210*, 803–810. [CrossRef]
56. Benjelloun, D.; Bonnet, J.; Doumerc, J.; Launay, J.; Onillon, M. Anisotropy in the electrical properties of zirconium doped α-Fe_2O_3 single crystals. *Mater. Chem. Phys.* **1988**, *20*, 1–12. [CrossRef]
57. Jamesh, M.I.; Wu, G.; Zhao, Y.; McKenzie, D.R.; Bilek, M.M.; Chu, P.K. Effects of zirconium and oxygen plasma ion implantation on the corrosion behavior of ZK60 Mg alloy in simulated body fluids. *Corros. Sci.* **2013**, *82*, 7–26. [CrossRef]
58. Rao, K.P.; Rao, A.U.M.; Gururaja, G.J. Effect of delta ferrite content on the corrosion resistance of type 316 clad metals. *Mater. Corros.* **1988**, *39*, 135–142. [CrossRef]
59. Örnek, C.; Leygraf, C.; Pan, J. Passive film characterisation of duplex stainless steel using scanning Kelvin probe force microscopy in combination with electrochemical measurements. *NPJ Mater. Degrad.* **2019**, *3*, 8. [CrossRef]
60. Zhu, S.; Huang, N.; Shu, H.; Wu, Y.; Xu, L. Corrosion resistance and blood compatibility of lanthanum ion implanted pure iron by MEVVA. *Appl. Surf. Sci.* **2009**, *256*, 99–104. [CrossRef]
61. Wu, H.; Xi, K.; Xiao, S.; Qasim, A.M.; Fu, R.K.; Shi, K.; Ding, K.; Chen, G.; Wu, G.; Chu, P.K. Formation of self-layered hydrothermal coating on magnesium aided by titanium ion implantation: Synergistic control of corrosion resistance and cytocompatibility. *Surf. Coat. Technol.* **2020**, *401*, 126251. [CrossRef]

62. Jamesh, M.; Wu, G.; Zhao, Y.; Chu, P.K. Effects of silicon plasma ion implantation on electrochemical corrosion behavior of biodegradable Mg–Y–RE Alloy. *Corros. Sci.* **2012**, *69*, 158–163. [CrossRef]
63. Gwinner, B.; Badji-Bouyssou, H.; Benoit, M.; Brijou-Mokrani, N.; Fauvet, P.; Gruet, N.; Laghoutaris, P.; Miserque, F.; Robin, R.; Tabarant, M. Corrosion of Zirconium in the Context of the Spent Nuclear Fuel Reprocessing Plant. In Proceedings of the GLOBAL 2015—21st International Conference and Exhibition Nuclear Fuel Cycle for a Low-Carbon Future, Paris, France, 20–24 September 2015; p. 5265. Available online: https://hal-cea.archives-ouvertes.fr/cea-02491643 (accessed on 1 April 2022).
64. Robin, R.; Miserque, F.; Spagnol, V. Correlation between composition of passive layer and corrosion behavior of high Si-containing austenitic stainless steels in nitric acid. *J. Nucl. Mater.* **2008**, *375*, 65–71. [CrossRef]
65. Sabot, R.; Devaux, R.; De Becdelievre, A.; Duret-Thual, C. The resistance to localized corrosion in neutral chloride medium of an AISI 304l stainless steel implanted with nitrogen and neon ions. *Corros. Sci.* **1992**, *33*, 1121–1134. [CrossRef]